The core helium flash revisited

I. One and two-dimensional hydrodynamic simulations

M. Mocák, E. Müller, A.Weiss, and K.Kifonidis

Max-Planck-Institut für Astrophysik, Postfach 1312, 85741 Garching, Germany
e-mail: mmocak@mpa-garching.mpg.de

Received ....

ABSTRACT

Context. We investigate the hydrodynamics of the core helium flash near its peak. Past research concerned with the dynamics of this event is inconclusive. However, the most recent multidimensional hydrodynamic studies suggest a quiescent behavior and seem to rule out an explosive scenario.
Aims. Previous work indicated, that depending on initial conditions, employed turbulence models, grid resolution, and dimensionality of the simulation, the core helium flash leads either to the disruption of a low-mass star or to a quiescent quasi-hydrostatic evolution. We try to clarify this issue by simulating the evolution with advanced numerical methods and detailed microphysics.
Methods. Assuming spherical or axial symmetry, we simulate the evolution of the helium core of a $1.25M_\odot$ star with a metallicity Z=0.02 during the core helium flash at its peak with a grid-based hydrodynamics code.
Results. We find that the core helium flash neither rips the star apart, nor that it significantly alters its structure, as convection plays a crucial role in keeping the star in hydrostatic equilibrium. In addition, our simulations show the presence of overshooting, which implies new predictions concerning mixing of chemical species in red giants.

Key words. Stars: evolution – hydrodynamics – convection – overshooting – Stars: red giants

1. Introduction

In stars of mass $0.7\ M_\odot \leq M \leq 2.2\ M_\odot$ the onset of helium burning constitutes a major event – the core helium flash. The pre-flash stellar core contains a white dwarf-like degenerate structure with a central density of about 10^6 g cm^{-3}, and an off-center temperature maximum resulting from plasma- and photo-neutrino cooling. When helium burning commences in this degenerate core, the liberated nuclear energy cannot be used to expand and cool the layers near the temperature maximum. Instead it causes further heating and a strong increase of the nuclear energy release. Only when convection sets in, part of the excess energy can be transported away from the burning regions, inhibiting thereby a thermonuclear explosion. At the end of the flash, the core has been expanded to densities of the order of 10^4 g cm^{-3}, with helium burning quiescently in the center, and the star has settled on the horizontal branch. While standard stellar evolution calculations have been very successful in reproducing observations of stars on the main sequence and the red giant branch (RGB), we are forced to recognize several discrepancies concerning the post-flash phases. In particular, we recall the lack of understanding of the horizontal-branch morphology, of low-luminosity carbon stars, and of hydrogen-deficient stars. Since all these (and other) problems appear after the RGB phase, it is plausible to suspect that the helium flash may be treated incorrectly in standard (hydrostatic) stellar evolution calculations.

The conceptual problems associated with the helium core flash arise from the extremely short timescales involved in the event. While the pre-flash evolution proceeds on a nuclear timescale of $\sim 10^8$ yrs, typical e-folding times for the energy release from helium burning can become as short as hours at the peak of the flash. Such short times are comparable to con-vective turnover times, *i.e.,* the common assumptions used for the treatment of convection in stellar evolution codes (instantaneous mixing, time-independence) are no longer valid. In addition, the assumption of hydrostatic equilibrium no longer needs to be fulfilled. Early attempts to overcome these assumptions by allowing for one-dimensional hydrodynamic flow (Edwards 1969; Zimmermann 1970; Villere 1976; Wickett 1977) remained inconclusive. The results ranged from a confirmation of the standard picture to a complete disruption of the star.

Cole & Deupree (1980, 1981) performed a two-dimensional hydrodynamic study of the core helium flash. However, their study was limited by the computational resources available at that time to a rather coarse computational grid (23 × 4 zones), a diffusive first-order difference scheme (weighted donor cell), and a short time evolution (10^5 s compared to the duration of the core helium flash of 10^{11} s from the onset of convection). They observed, at the radius of the off-center temperature maximum, a series of thermonuclear runaways where heat transport by convection and conduction was sufficiently efficient to limit the rise of temperature. Each runaway modified the convective flow pattern and led to some inward transport of heat across the off-center temperature inversion. During the simulation the time interval between runaways continuously shortened, and the maximum temperature steadily increased until it eventually exceeded $10^9 K$.

Deupree & Cole (1983) and (Deupree 1984a,b) confirmed these findings using two-dimensional models with an improved angular resolution (6° instead of 20°), and three-dimensional simulations (with 8×8 angular zones in a 80°×80° cone, *i.e.,* 10° angular resolution). Cole et al. (1985) performed stellar evolution calculations of the core helium flash using a model for convective overshooting based on these hydrodynamic simula-
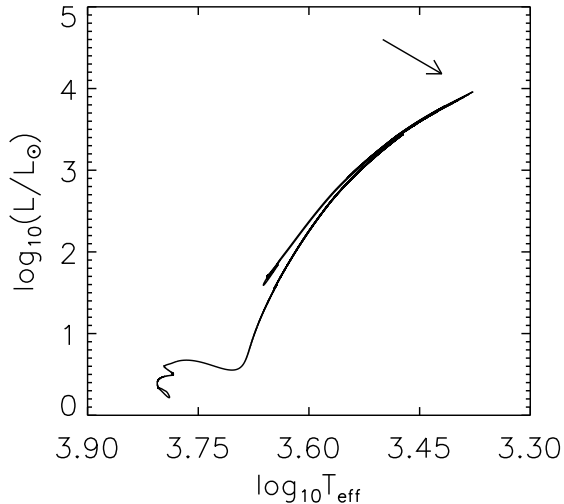
Fig. 1. Theoretical evolutionary track of a 1.25 $M_\odot$ star with a metallicity Z=0.02 in the H-R diagram. The core helium flash begins at the tip of the red giant branch indicated by the arrow.

Fig. 2. Temperature distribution as a function of radius. The dashed line gives the distribution obtained from stellar evolutionary calculations with the "Garstec" code, while the solid line shows the mapped and stabilized distribution used as initial condition in the hydrodynamic simulations. CVZ marks the convection zone.

tions. They found that the evolution of the core helium flash is unchanged except for about the last week prior to its peak. Furthermore, the possibility of mixing of core material into the hydrogen shell was suggested by numerical experiments where point source explosions were enforced (Deupree 1984b, 1986; Deupree & Wallace 1987). These results raised the hope that some problems concerning abundance anomalies and mass loss could be solved by understanding the core helium flash.

The results of the hydrodynamic simulations, though varying in details, indicated a dynamic flash that could disrupt the star (Deupree 1984a) or at least lead to a significant loss of the envelope (Cole & Deupree 1981). The simulations were critized by Iben & Renzini (1984) and Fujimoto et al. (1990) because (i) the radial grid was too coarse, (ii) the gravitational potential was "frozen in" (*i.e.,* time-independent), and (iii) because a "closed" outer boundary was used. The latter two assumptions tend to underestimate the expansion of the core, and hence tend to overestimate the violence of the flash.

Since the work of Deupree the computational capabilities have grown tremendously and methods to simulate hydrodynamic flow have improved considerably. Thus, the limitations of the early studies concerning the grid resolution and the numerical treatment, which were the main points of critique, meanwhile can be reduced considerably. At the same time, we still have no coherent picture up to what extent and under what circumstances (stellar mass and composition) hydrodynamic core helium flash evolution could differ from canonical stellar evolution calculations. It therefore appears necessary to have a new and fresh look into the dynamics of the core helium flash. Incidentally, Deupree (1996) himself re-examined the problem already more than a decade ago concluding that the flash does not lead to any hydrodynamic event. Quiescent behavior of the core helium flash is also favored by recent three-dimensional simulations (Dearborn et al. 2006; Lattanzio et al. 2006) where the energy transport due to convection, heat conduction, and radiation seems to be always able to transport most of the energy generated during the flash quiescently from the stellar interior to the outer stellar layers, implying no hydrodynamic event, and hence a quasi-hydrostatic evolution.
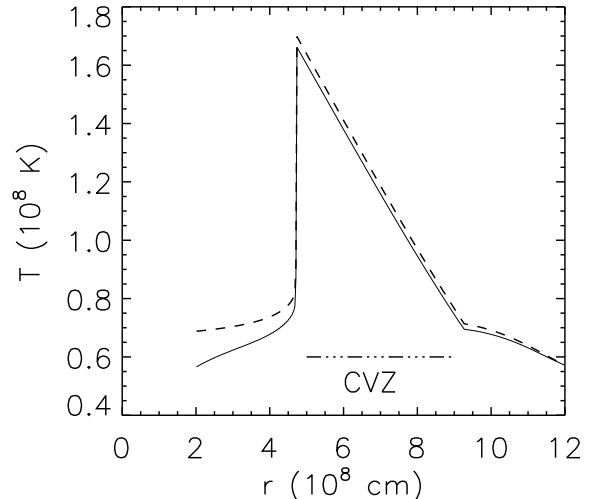
In the following we present a completely independent investigation of the core helium flash by means of one-dimensional and two-dimensional hydrodynamic simulations using state-of-the-art numerical techniques, a detailed equation of state, and a time-dependent gravitational potential. The hydrodynamic calculations cover about 8 hrs of the evolution near the peak of the core helium flash. In passing we note that the present investigation was instigated by a similar, meanwhile technically obsolete study which was performed by Kurt Achatz (Achatz 1995) in the context of his diploma thesis. The results of this latter study have unfortunately never been published.

The paper is organized as follows. In Sect. 2 we discuss briefly the stellar input model for the simulations along with some results from hydrostatic core helium flash calculations. In Sect. 3 the hydrodynamics code and the numerical methods are introduced, while the results of our one and two-dimensional hydrodynamic runs are presented in Sect. 4 and 5, respectively. Finally, the conclusions are given in Sect. 6.

2. Initial stellar models and hydrostatic calculations

Table 1 summarizes some properties of our initial model, which was obtained from stellar evolutionary calculations with the "Garstec" code (Weiss & Schlattl 2000, 2007). It corresponds to a star with a mass of 1.25 $M_\odot$ and a metallicity Z = 0.02 at the peak of the core helium flash ($L_{He} \sim 10^9 L_\odot$) evolved with a hydrostatic stellar evolution code. During this violent episode, the star is located at the tip of the red giant branch in the H-R diagram (Fig. 1), hence being a red giant consisting of a small central helium core with a radius $r \sim 1.9\,10^9$ cm, surrounded by a hydrogen burning shell and a huge convective envelope with a radius r $\sim 10^{13}$ cm. Figure 2 shows the temperature distribution inside the helium core, which is characterized by an off-center temperature maximum T_{max}, from where the temperature steeply drops towards smaller radii and follows a super-adiabatic gradient towards larger radii (convection zone). The radius r_{max}

Table 1. Some properties of the initial model: total mass M, stellar population, metal content Z, mass M_{He} and radius R_{He} of the helium core ($X(^4He) > 0.98$), nuclear energy production in the helium core L_{He}, maximum temperature of the star T_{max}, and radius r_{max} and density ρ_{max} at the temperature maximum.

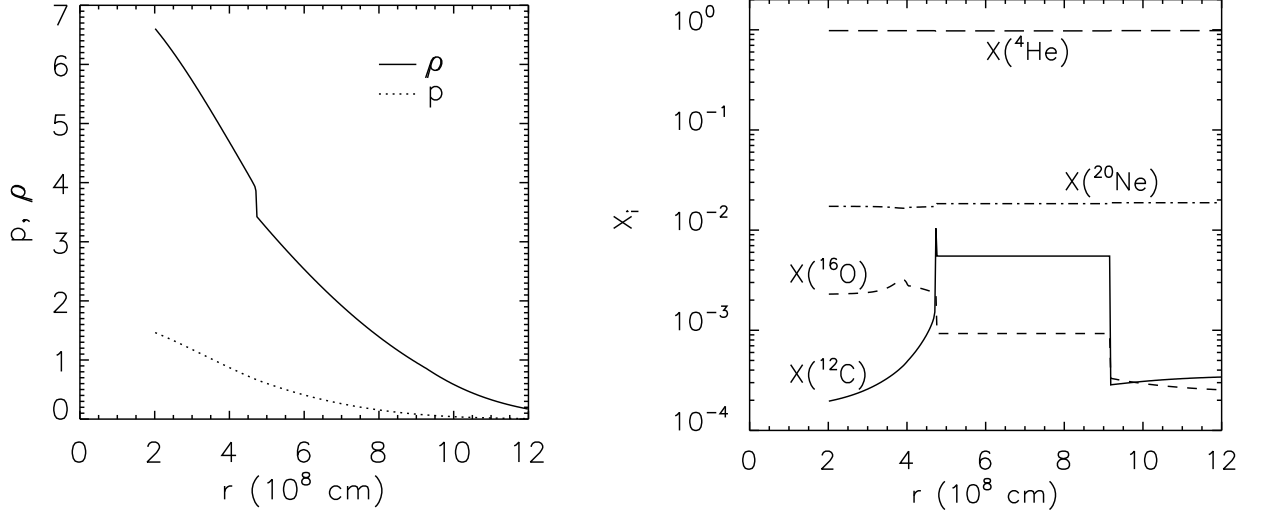| Model	M [$M_\odot$]	Pop.	Z	M_{He} [$M_\odot$]	R_{He} [10^9 cm]	L_{He} [$10^9 L_\odot$]	T_{max} [10^8 K]	r_{max} [10^8 cm]	ρ_{max} [10^5 g cm^{-3}]
M	1.25	I	0.02	0.38	1.91	1.03	1.70	4.71	3.44

Fig. 3. *Left panel:* Pressure (in 10^{22} dyn cm^{-2}) and density (in 10^5 g cm^{-3}) distribution of the mapped and stabilized initial model. The pressure and density profile of the original stellar evolution cannot be distinguished from the profiles of the mapped model on this scale. *Right panel:* Chemical composition of the initial model showing a dominant fraction of helium and an apparent peak in ^{12}C at the position of the temperature maximum resulting from a non-instantaneous treatment of convective mixing.

of the temperature maximum coincides with the bottom of the convection zone. The almost discontinuous temperature stratification near T_{max} (temperature inversion), where the temperature rises from $7\,10^7$K to $1.7\,10^8$K, results from an interplay between neutrino cooling and heating by nuclear burning. Figure 3 shows the density and pressure stratification of the model. One recognizes that the temperature inversion is correlated with a drop in density. A detailed view reveals that the steep increase of temperature corresponds to a decrease of the density by 11%, an increase of the ion pressure by 70%, and a drop of the electron pressure by 9%, respectively. Even at the peak of the core helium flash, the helium core is still strongly degenerate: compared to the electron pressure the ion pressure is lower by a factor of 6, while the radiation pressure is smaller by almost 3 orders of magnitude.

The stellar model contains the chemical species ^{1}H, ^{3}He, ^{4}He, ^{12}C, ^{13}C, ^{14}N, ^{15}N, ^{16}O ,^{17}O, ^{24}Mg, and ^{28}Si. However, since we are here not interested in the detailed chemical evolution of the star, it is not necessary to consider all of these species in our hydrodynamic simulations, as the triple-α reaction dominates the energy production rate during the core helium flash. For our hydrodynamic simulations we thus adopt only the abundances of ^{4}He, ^{12}C, and ^{16}O. The remaining composition is assumed to be adequately represented by a gas with a mean molecular weight equal to that of ^{20}Ne (Fig. 3).

The stellar evolutionary model is one-dimensional, hydrostatic, and was computed on a Lagrangian grid of 2294 zones. Since only the helium core of the model (without its very central part; see Sect. 3.6) is of interest to us, we consider only the

initial data for $2\,10^8$ cm $\leq r \leq 1.2\,10^9$ cm, and interpolate all relevant quantities (*e.g.,* density, temperature, composition) onto our Eulerian, lower resolution computational grid using polynomial interpolation (Press et al. 1992). Due to the interpolation errors and subtle differences in the input physics, the interpolated model is no longer in perfect hydrostatic equilibrium. In order to perfectly balance also the gravitational and pressure forces in the interpolated model, we use an iterative procedure in the first hydrodynamic timestep to minimize the numerical fluxes across zone boundaries. The whole process results in a small temperature decrease with respect to the temperature profile of the original model (Fig. 2). The differences do not exceed a few percent depending on the radial resolution of the Eulerian grid. The resulting changes in the density and pressure profiles are negligible due to the strong electron degeneracy of the gas. The main cause for the slight de-stabilization of the mapped initial stellar model is the use of different equations of state in both codes. The hydrodynamic code employs the equation of state by Timmes & Swesty (2000), whereas the "Garstec" code relies on the OPAL equation of state by Rogers et al. (1996). At a given density, temperature, and composition in the helium core during the flash, these equations of state give pressure values which differ typically by 1 % the difference being most apparent in regions where the matter is highly degenerate.

Given that the maximum temperature in the helium core is $T \sim 1\,10^8K$, the stellar model reaches the peak in nuclear energy production rate during the core helium flash in less than 10^4 yrs. The rate at which the nuclear energy production rises is highly non-linear. From the onset of the core helium flash at a
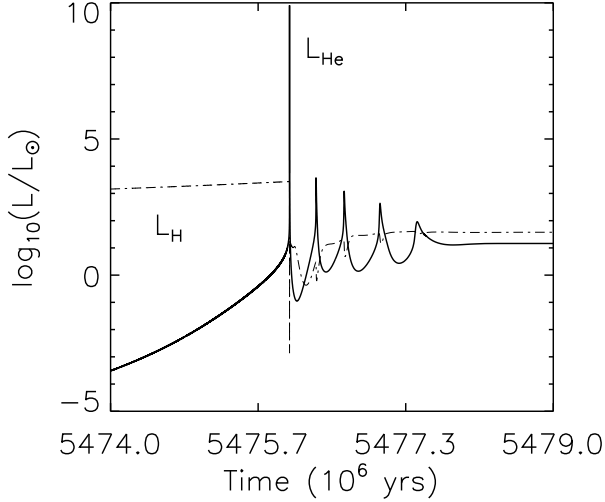
Fig. 4. Temporal evolution of the helium luminosity L_{He} (solid) versus the hydrogen luminosity L_H (dash-dotted) of model M during the core helium flash.

helium luminosity $L_{He} \sim 10^1 L_\odot$, it takes almost 30000 yrs to reach $L_{He} \sim 10^4 L_\odot$, whereas it requires only 40 yrs to reach $L_{He} \sim 10^{10}$. The first core helium flash is followed by four subsequent mini flashes (Fig. 4) identified as thermal pulses by Thomas (1967) until the degeneracy in the helium core is lifted completely and the star settles down on the horizontal branch quiescently burning helium in its core.

Since the computed model is a Pop I metal rich star, it does not experience any hydrogen entrainment during the core helium flash (Fujimoto et al. 1990; Schlattl et al. 2001).

3. Input physics and numerics

3.1. Thermal transport

The energy flux density due to thermal transport is given by

$$f_{\text{cond}} = -K_{\text{cond}}\nabla T , \tag{1}$$

where K_{cond} is the total conductivity (erg K^{-1} cm^{-1} s^{-1}) and ∇T the temperature gradient.

In the helium core, which is partially degenerate, thermal transport due to both radiative diffusion and electron conduction is important, while heat transport by ions is negligible, *i.e.,*

$$K_{\text{cond}} = K_\gamma + K_e . \tag{2}$$

The radiative conductivity is given by

$$K_\gamma = \frac{4ac}{3}\frac{T^3}{\kappa_\gamma\rho} , \tag{3}$$

where κ, a, and c are the Rosseland mean of the opacity, the radiation constant, and the speed of light, respectively. For the opacity, we use a fit formula due to Iben (1975) which is based on the work by Cox & Stewart (1970b,a). It takes into account the radiative opacity due to Thomson scattering, free-free (Krames opacity), bound-bound, and bound-free transitions.

For the thermal transport by electron conduction we consider contributions due to electron-ion, and electron-electron collisions which are treated according to Yakovlev & Urpin (1980), and Potekhin et al. (1997).

3.2. Neutrino emission

The evolutionary time covered by our hydrodynamic simulations is too short for neutrino cooling to be of importance. The neutrino losses computed from the analytic fits of Itoh et al. (1996) give a cooling rate $\dot\epsilon < 10^2$ erg g^{-1} s^{-1}, or a corresponding decrease of the maximum temperature by $|\Delta T| < 10^{-1}$ K over the longest simulations we performed. Hence, cooling by neutrinos was neglected.

3.3. Equation of state

The equation of state employed in our hydrodynamic code includes contributions due to radiation, ions, electrons, and positrons. Thus, the total pressure is given by

$$P = P_\gamma + P_{ion} + P_e + P_p , \tag{4}$$

where

$$P_\gamma = \frac{a}{3}T^4 \tag{5}$$

is the radiation pressure of a black body of temperature T (a is the universal radiation constant), and

$$P_{ion} = \sum_i \Re\frac{\rho X_i}{A_i}T = \Re\rho T \sum_i Y_i \tag{6}$$

is the pressure of a non-relativistic Boltzmann gas of density ρ consisting of a set of ions of abundance $Y_i = X_i/A_i$ (X_i and A_i are the mass fraction and the atomic mass number of species i, respectively). $P_e + P_p$ is the pressure of an arbitrarily degenerate and relativistic electron-positron gas based on table interpolation of the Helmholtz free energy (Timmes & Swesty 2000).

3.4. Nuclear burning

The energy generation rate by nuclear burning is given by

$$\dot\varepsilon_{\text{nuc}} = \sum_i \frac{\Delta m_i c^2}{m_u}\dot Y_i \tag{7}$$

where

$$\Delta m_i = M_i - A_i m_u . \tag{8}$$

is the mass excess of a nucleus of mass M_i, and m_u is the atomic mass unit.
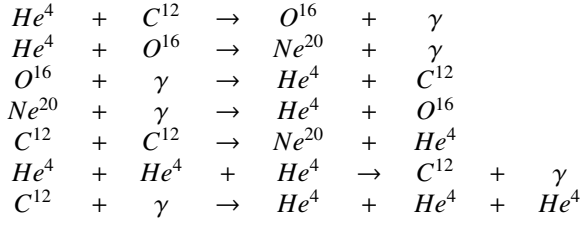
Abundance changes are described by a nuclear reaction network consisting of the four α-nuclei ^{4}He, ^{12}C, ^{16}O, and ^{20}Ne, coupled by seven reactions (including the triple-α reaction). We used the reaction rate library of Thielemann (private communication), which gives the product of the Avogadro number N_A and the velocity averaged cross section $\langle\sigma v\rangle$ in terms of the fit formula

$$N_A\langle\sigma v\rangle = \sum_{l=1}^{n_l} \exp\Big[c_{1l} + c_{2l}T^{-1} + c_{3l}T^{-1/3} + c_{4l}T^{1/3}$$
$$+ c_{5l}T + c_{6l}T^{5/3} + c_{7l}\ln T\Big] , \tag{9}$$

with rate dependent coefficients c_{il} ($1 \le i \le 7$). Up to three sets of coefficients (*i.e.,* $1 \le n_l \le 3$) are used. The total reaction rate due to all one body, two body, and three body interactions has the form (Müller 1998):

$$\dot Y_i = \sum_j c_i\lambda_j Y_j + \sum_{j,k} c_i(j,k)\rho N_A\langle\sigma v\rangle_{j,k}Y_j Y_k$$
$$+ \sum_{j,k,l} c_i(j,k,l)\rho^2 N_A^2\langle\sigma v\rangle_{j,k,l}Y_j Y_k Y_l , \tag{10}$$

where the weight factors c_i inhibit multiple counts in the sums over the nuclei j,k,l. The following nuclear reactions were considered:

$$
\begin{array}{ccccccccc}
He^4 & + & C^{12} & \rightarrow & O^{16} & + & \gamma \\
He^4 & + & O^{16} & \rightarrow & Ne^{20} & + & \gamma \\
O^{16} & + & \gamma & \rightarrow & He^4 & + & C^{12} \\
Ne^{20} & + & \gamma & \rightarrow & He^4 & + & O^{16} \\
C^{12} & + & C^{12} & \rightarrow & Ne^{20} & + & He^4 \\
He^4 & + & He^4 & + & He^4 & \rightarrow & C^{12} & + & \gamma \\
C^{12} & + & \gamma & \rightarrow & He^4 & + & He^4 & + & He^4
\end{array}
$$

Mathematically this results in a nuclear reaction network consisting of seven non-linear first order differential equations of the form given by Eq. (10) and a temperature equation

$$
\frac{\partial T}{\partial t} = \dot{\varepsilon}_{nuc} \frac{\partial T}{\partial \varepsilon}, \tag{11}
$$

where ε is the specific internal energy.

The effects of electron screening were included according to Dewitt et al. (1973) for the triple-α reaction rate, and in the weak screening regime only.

3.5. Evolutionary equations

The hydrodynamic and thermonuclear evolution of the core helium flash was computed by solving the governing set of fluid dynamic equations in spherical coordinates on an Eulerian grid. Using vector notation these equations have the form,

$$
\frac{\partial \mathbf{U}}{\partial t} + \nabla \mathbf{F} = \mathbf{S} \tag{12}
$$

with the state vector $\mathbf{U}$

$$
\mathbf{U} \equiv \begin{pmatrix} \rho \\ \rho \mathbf{v} \\ \rho e \\ \rho Y_i \end{pmatrix} \tag{13}
$$

the flux vector $\mathbf{F}$

$$
\mathbf{F} \equiv \begin{pmatrix} \rho \mathbf{v} \\ \rho \mathbf{v}\mathbf{v} \\ (\rho e + p)\mathbf{v} + f_{cond} \\ \rho Y_i \mathbf{v} \end{pmatrix} \tag{14}
$$

and the source vector $\mathbf{S}$

$$
\mathbf{S} \equiv \begin{pmatrix} 0 \\ -\rho \nabla \Phi \\ -\rho \mathbf{v} \cdot \nabla \Phi + \rho \dot{\varepsilon}_{nuc} \\ \rho \dot{Y}_i \end{pmatrix} \tag{15}
$$

with $i = 1, \ldots, N_{nuc}$ where N_{nuc} is the number of nuclear species considered in the nuclear reaction network, and ρ, p, $\mathbf{v}$ and Φ are the density, pressure, velocity and gravitational potential. respectively. The term f_{cond} describes energy transport by thermal conduction (see Sect. 3.1), and $\dot{\varepsilon}_{nuc}$ and the $\dot{Y}_i$ are the nuclear energy generation rate and the change of the mass fraction of species i due to nuclear reactions, respectively (see Sect. 3.4). The total energy density $\rho e = \rho \varepsilon + \rho \mathbf{v}\mathbf{v}/2$ with e being the specific total energy.

3.6. Code

The numerical simulations were performed with a modified version of the hydrodynamic code Herakles (Kifonidis et al. 2003, 2006), which is a descendant of the code Prometheus developed by Bruce Fryxell and Ewald Müller (Müller et al. 1991; Fryxell et al. 1991). The hydrodynamic equations are integrated to second order accuracy in space and time using the dimensional splitting approach of Strang (1968), the PPM reconstruction scheme (Colella & Woodward 1984), and a Riemann solver for real gases according to Colella & Glaz (1984). The evolution of the chemical species is described by a set of additional continuity equations (Plewa & Müller 1999). Source terms in the evolutionary equations due to self-gravity and nuclear burning are treated by means of operator splitting. Every source term is computed separately, and its effect is accounted for at the end of the integration step. The viscosity tensor is not taken into account explicitly, since the solution of the Euler equations with the PPM scheme corresponds to the use of a sub-grid scale model that reproduces the solution of the Navier-Stokes equations reasonably well (Meakin & Arnett 2007). Thermal transport is treated in a time-explicit fashion when integrating the evolutionary equations. Self-gravity is implemented according to Müller & Steimnetz (1995), while the gravitational potential is approximated by a one-dimensional Newtonian potential which is obtained from the spherically averaged mass distribution. The nuclear network is solved with the semi-implicit Bader-Deufelhard method which utilizes the Richardson extrapolation approach and sub-stepping techniques (Bader & Deuflhard 1983; Press et al. 1992) allowing for very large effective time steps.

The code is vectorized and allows for an adjustment of the vector length to the memory architecture. Therefore, an optimal performance on both vector and super-scalar, cache-based machines can be achieved.

A program cycle consists of two hydrodynamic timesteps and proceeds as follows:

1. The hydrodynamic equations are integrated in r-direction (r-sweep) including the effects of heat conduction. The time averaged gravitational forces are computed, and the momentum and the total energy are updated to account for the gravitational source terms. Subsequently, the equation of state is called to update the thermodynamic state due to the change of the total energy.
2. Step (1) are repeated in θ-direction (θ-sweep).
3. The nuclear network is solved in all zones with significant nuclear burning (T > 10^8 K). Subsequently, the equation of state is called to update the pressure and the temperature.
4. In the subsequent timestep the order of Step (1) and (2) is reversed to guarantee second-order accuracy of the time integration, and Step (3) is repeated with the updated quantities.
5. The size of the timestep for the next cycle is determined.

When using spherical coordinates, the CFL stability condition on the timestep is most restrictive near the origin of the grid. However, inside a region beneath the off-center temperature maximum there are no significant non-radial motions to be expected during the evolution of the core helium flash except in the immediate vicinity of the temperature inversion, where convective overshooting may occur. Hence, cutting out the very center of the computational grid does not lead to any numerical bias, but saves considerable amounts of computational time. In the radial direction we used a closed (i.e., reflective) outer and inner quasi-hydrostatic boundary obtained by means of polynomial extrapolation, which significantly suppresses any artificial
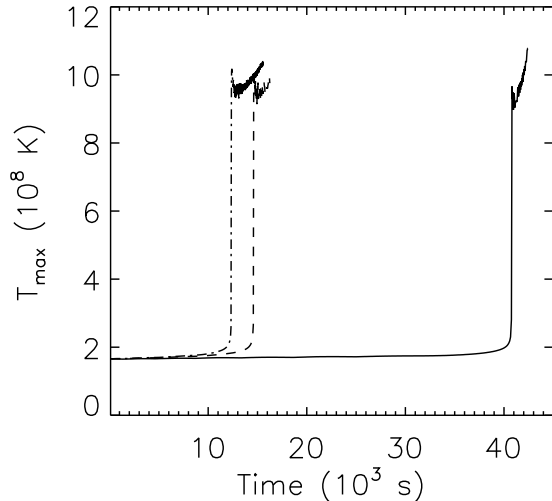
Fig. 5. Evolution of the temperature maximum T_{max} in the one-dimensional models JE2 (solid), JE3 (dashed), and JE4 (dash-dotted), respectively.
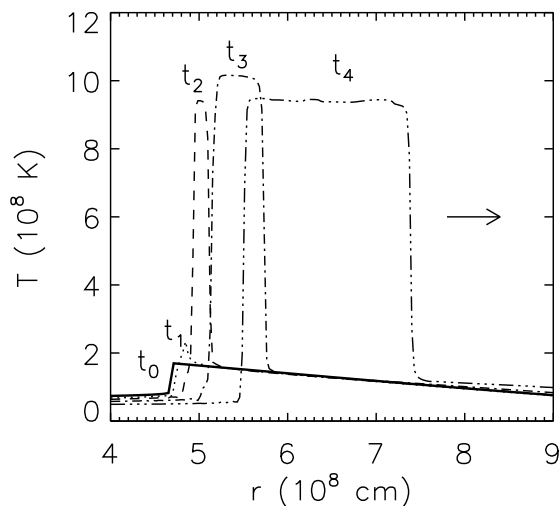

Fig. 6. Temperature stratification across the helium core in model JE4 during the runaway at $t_1 = 12270$ s (dotted), $t_2 = 12352$ s (dashed), $t_3 = 12392$ s (dash-dotted), and $t_4 = 12762$ s (dash-dot-dotted), respectively. The solid line corresponds to the initial model (t_0), and the arrow indicates the direction of the flame propagation.

velocity fluctuations resulting from an imbalance of gravitational and pressure forces in the boundary zones. For two-dimensional runs, the boundary conditions in the angular direction are reflective as well.

After interpolation and stabilization, the initial model in the two-dimensional simulations had to be perturbed explicitly to trigger convection, because an initially exactly spherically symmetric model remains that way for ever when evolved in spherical coordinates with our code. We imposed a random flow field with a maximum (absolute) velocity of 10 cm s^{-1}, and random density perturbations with $\Delta\rho/\rho \leq 10^{-2}$.

4. Results of 1D simulations

Table 2. Some properties of the 1D simulations: number of radial grid points (N_r), radial resolution (Δr in 10^8cm), time up to the thermonuclear runaway, t_{trn}, and maximum evolution time t_{max} (both in s).

run	N_r	Δr	t_{trn}	t_{max}
JE2	180	5.55	40700	42500
JE3	270	3.77	14600	16250
JE4	360	2.77	12300	15600

We have performed several one-dimensional simulations using model M, which differ only by their grid resolution (see Table 2) to see whether without allowing for convective flow a thermonuclear runaway can be avoided.

Figure 5 demonstrates that heat conduction and adiabatic expansion alone fail to stabilize the model, *i.e.,* one-dimensional hydrodynamic simulations result in a thermonuclear runaway. Initially, the maximum temperature increases only slowly, but it starts to rise rapidly after a time t_{trn} (Tab. 2) up to a value $T \sim 10^9$ K. For instance, from the temperature evolution of model JE4 one can determine that a local hot spot with a temperature of $2.3\,10^8$ K will runaway after about 80 s (Fig. 6). The time at which the runaway is triggered depends on the grid resolution, being longer in models with lower resolution (Fig. 5).

In every case, a thermonuclear flame with $T \sim 10^9$ K ultimately forms and propagates outwards with a subsonic velocity depending on the grid resolution. Since our two-dimensional (more realistic) simulations do not show such a behavior, we will refrain from further discussing details of the one-dimensional simulations.

5. Results of 2D simulations

In Table 3 we summarize some characteristic parameters of our two-dimensional simulations that are based on model M.

We will first discuss one specific simulation DV4 in some detail, which serves as a standard to which we will compare the results of other runs. Thereafter, we will discuss some general properties of all 2D simulations. Every simulation covered approximately 30000 s ($\sim$ 8 hrs) of the evolution near the peak of the core helium flash. They were performed on an equidistant spherical grid encompassing 95% of the helium core's mass (X(^{4}He)>0.98) except for a central region with a radius of $r = 2\,10^8$ cm which was excised in order to allow for larger timesteps. As this radius is sufficiently smaller than the radius of the temperature inversion ($r \sim 5\,10^8$ cm), its presence does not influence the convection zone.

5.1. Simulation DV4

After the start of the simulation the initial velocity perturbations begin to grow in a narrow layer just outside the temperature maximum ($r \sim 5\,10^8$ cm), *i.e.,* in the region heated by nuclear burning. Later on at t $\sim$ 800 s, several hot bubbles appear, which rise upward with maximum velocities $\sim 4\,10^6$ cm s^{-1} (Fig. 8). They are typically about 0.2% hotter than the angular averaged temperature at a given radius. The ^{4}He mass fraction of all hot bubbles is about 0.4% less than the corresponding angular averaged value since helium has been depleted in the bubbles by the

Table 3. Some properties of the 2D simulations: number of grid points in radial (N_r) and angular (N_θ), radial (Δr in 10^8cm) and angular grid resolution ($\Delta\theta$), characteristic length scale l_c of the flow (in 10^8cm), characteristic velocity v_c of the flow (in 10^6 cm s^{-1}), Reynolds number R_n associated with the numerical viscosity of our code (Porter & Woodward 1994), damping time-scale due to the numerical viscosity t_n, typical convective turnover time t_o, and maximum evolution time t_{max} (in s), respectively.

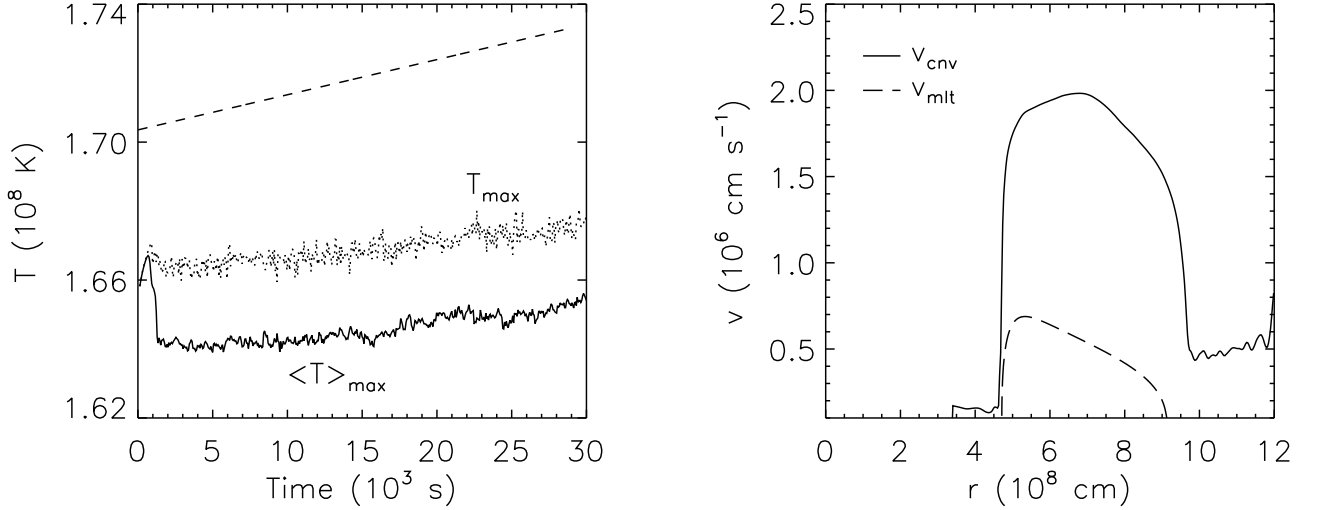| run	grid	Δr	$\Delta\theta$	l_c	v_c	R_n	t_n	t_o	t_{max}
DV2	180×90	5.55	2°	4.7	1.03	1900	11000	910	30000
DV3	270×180	3.70	1°	4.7	1.46	8900	36000	640	30000
DV4	360×240	2.77	0.75°	4.7	1.52	21000	83000	620	30000

Fig. 7. *Left panel:* Temporal evolution of the horizontally averaged temperature maximum $\langle T \rangle_{max}$ (solid), and of the global temperature maximum T_{max} (dotted) in model DV4. The dashed line corresponds to the temporal evolution of the maximum temperature in the stellar evolutionary calculations of the model M. *Right panel:* The r.m.s convection velocity v_{cnv} in simulation DV4 averaged over 6000 s (solid) versus the convection velocity predicted by the mixing length theory v_{mlt} (dashed).

triple α reaction. Consequently, ^{12}C and ^{16}O (produced in helium burning) are enhanced by $\sim 0.7\%$ in the bubbles.

During the first 700 s of the evolution, the off-center maximum mean temperature $\langle T \rangle_{max}$ rises with a rate of ~ 1000 K s^{-1} until it reaches a value $\sim 1.67\,10^8\,K$. At this moment, from the region around the $\langle T \rangle_{max}$, the bubbles emerge and cause its decrease by $\sim 2.6\,10^6\,K$ in just 570 s corresponding to a temperature drop rate of 4540 K s^{-1} (Fig. 7). This phase marks the onset of convection where a fraction of the thermonuclear energy released via helium burning starts to be efficiently transported away from the burning regions by matter flow, thereby inhibiting a thermonuclear runaway.

Once the bubbles form, they rise upwards and start to interact and merge, *i.e.,* the convective layer begins to grow in radius. About ~ 1300 s after the start of the simulation, the whole convection zone is covered by an almost stationary flow pattern with an almost constant total kinetic energy of the order of 10^{45} erg. At this time vortices dominate the flow pattern. They extend across the whole convective region ($\sim 2.1 H_p$), and are of approximately similar angular size, one vortex covering about 40 degrees (diameter $\sim 5\,10^8$ cm). Usually we find about four such vortices with two dominant up-flows of hot gas at $\theta \sim 60°$, and $\theta \sim 120°$, respectively (see, *e.g.,* Fig. 8). These large vortices are rather stable surviving until the end of our simulations. Typical convective flow velocities are $v_{cnv} \sim 1.5\,10^6$ cm s^{-1}, and thus well below the local sound speed ($c_S \sim 1.7\,10^8$ cm s^{-1}), *i.e.,* a

vortex requires about 600 s for one rotation. The persistence of vortices is not typical for turbulent convection.

The dominance of large scale structures might be a consequence of the usage of a Riemann solver based compressible code. The Mach number M of the convective flow is ~ 0.01. Is PPM suited for this kind of subsonic flow? This question, which is beyond the scope of the present study, needs to be investigated, as it is know that the artificial viscosity of standard Riemann solver methods exhibit incorrect scaling with the flow Mach number as $M \rightarrow 0$. (Turkel 1999) *i.e.,* the inherent artificial viscosity of PPM may be too high for adequately simulating flows at low Mach numbers (*e.g.,* $M \sim 0.01$).

Energy transport by convection within the vortices is concentrated into a few narrow upward drafts, compensated partially, but only to a small extent, by down-flows. The vortices transport energy mostly along their outer edges. Matter in their centers does not interact with regions of dominant nuclear energy production at all.

The horizontally averaged value of the maximum temperature, barring some additional temperature fluctuations due to convection, is slightly rising after the onset of convection during the whole subsequent evolution with a rate of around 40 K s^{-1} (see Fig. 7). This rate seems to be about 60% smaller than the rate seen in the stellar evolutionary calculations (~ 100 K s^{-1}), which could be either a result of the initially lower value of the temperature maximum after the stabilization phase at the begin-
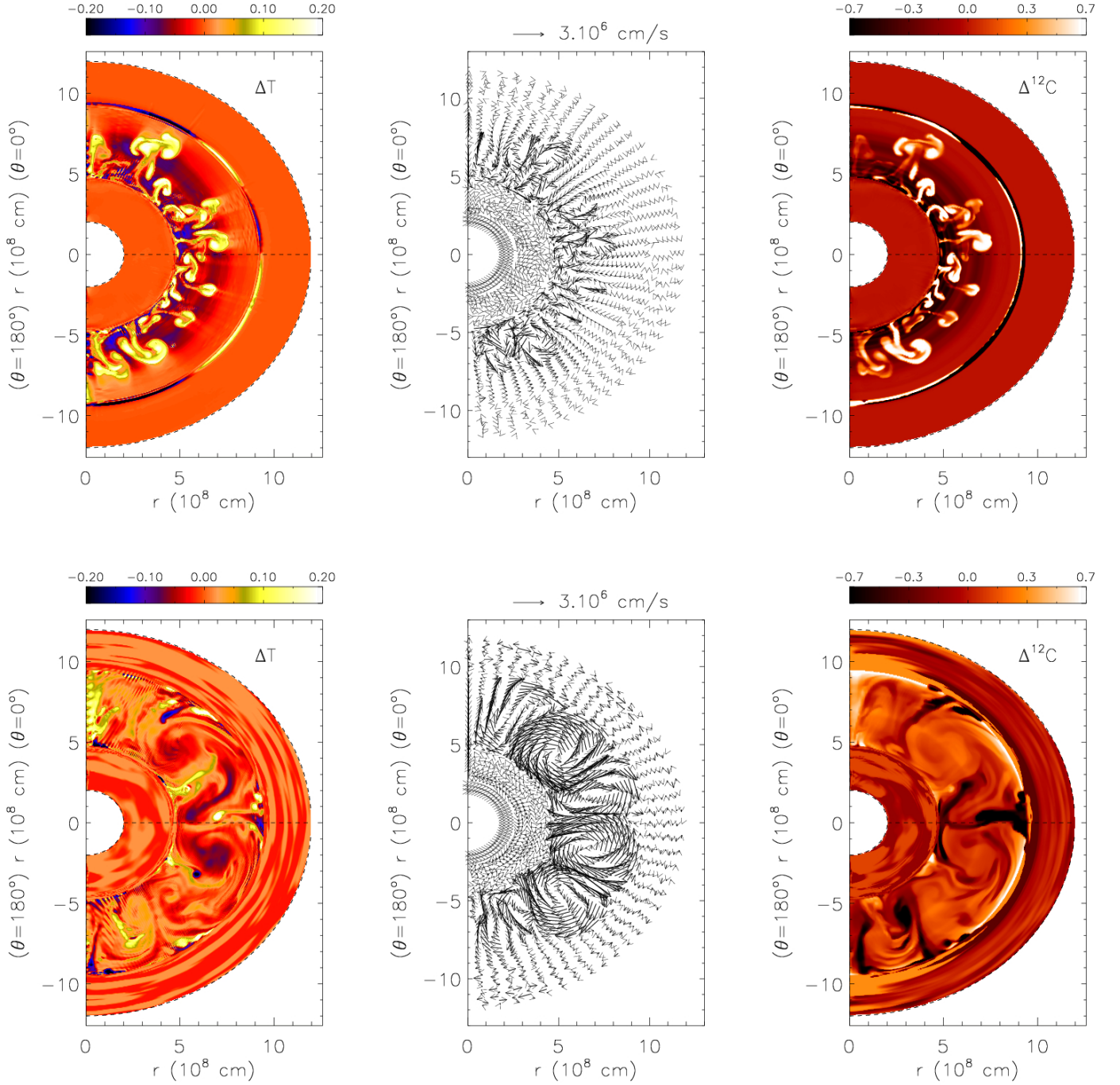
Fig. 8. Snapshots of the onset of convection at $1020\,s$ (upper panels), and of the evolved convection at $29000\,s$ (lower panels) in model DV4, showing the temperature contrast $\Delta T = 100\,(T - \langle T\rangle_\theta)/\langle T\rangle_\theta$ (left panels), the velocity field (middle panels), and the ^{12}C contrast $\Delta^{12}C = 100\,(^{12}C - \langle^{12}C\rangle_\theta)/\langle^{12}C\rangle_\theta$ (right panels), respectively. $\langle\rangle_\theta$ denotes a horizontal average at a given radius.

ning of the simulation (see Sec. 2) or more dynamic convective motion, since the mean convective velocities v_{cnv} exceed the velocities predicted by mixing length theory, v_{mlt}, on average by a factor of four (Fig. 7).

Convection distributes the energy in such a way that the temperature gradient ∇ never significantly exceeds ∇_{ad} in model M. Although, the value of ∇ established at the beginning of the simulation deviates slightly after some time from the gradient at later times, it remains close to the adiabatic temperature gradient ∇_{ad} (the relative difference is less than 1%). In this respect

there is thus no indication of any significant deviation from the situation obtained in stellar evolutionary calculations.

The apparent spike in the initial ^{12}C distribution at the location of the temperature maximum (Fig. 3) is a result of a non-instantaneous treatment of the convective mixing in stellar evolutionary calculations. It turns out that a non-instantaneous treatment of mixing is not required during the core helium flash since simulation DV4 indicates that the spike gets smeared out immediately after convection is triggered. This implies that the assumption of instantaneous mixing is a good approximation lo-
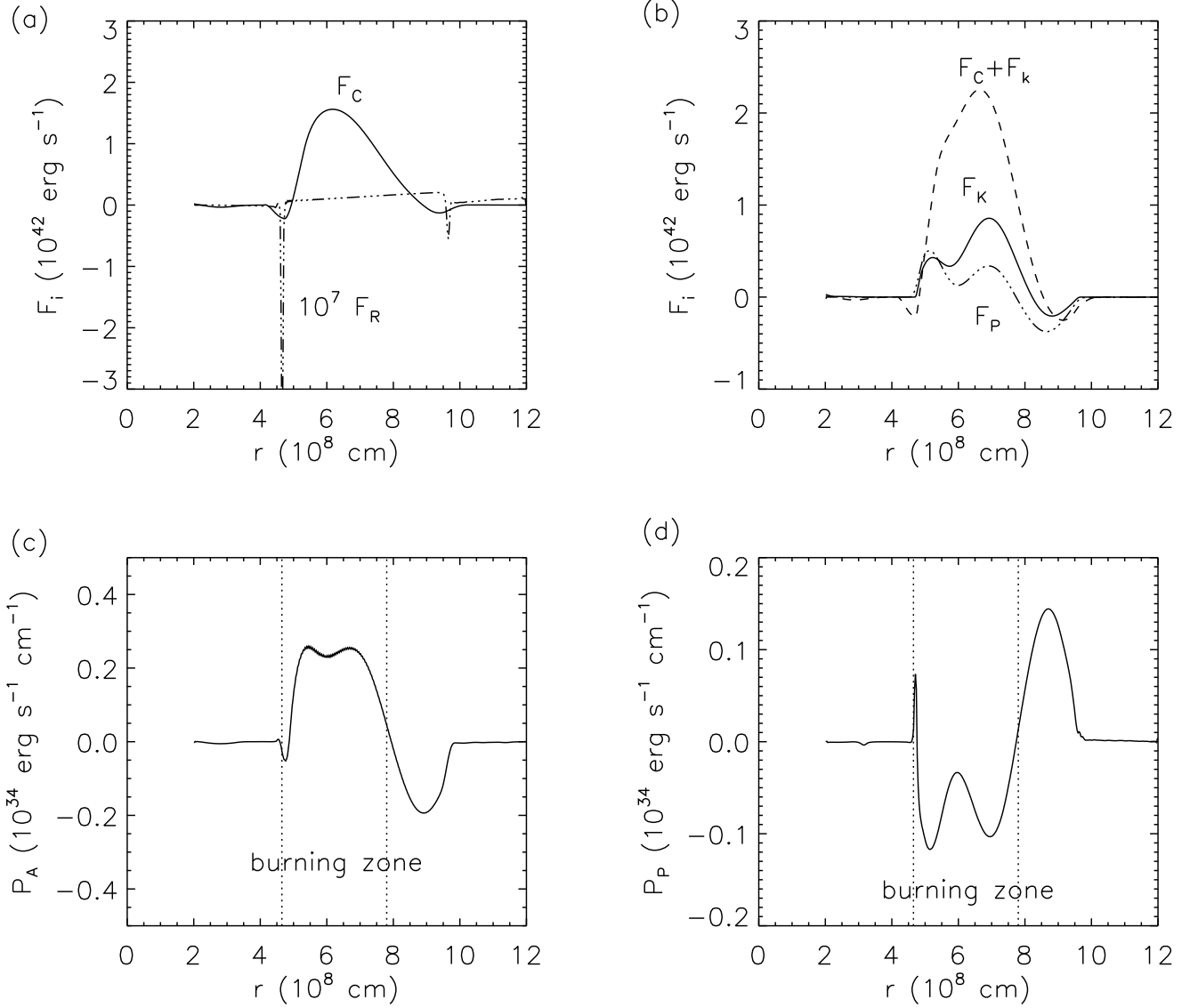
Fig. 9. Snapshots of various energy fluxes and source terms in model DV4 (time averaged over 6000 s from $t = 18000$ s to $t = 24000$ s): (a) convective flux F_C (solid), and the energy flux due to the thermal transport F_R (dash-dotted); (b) kinetic flux F_K (solid), acoustic flux F_P (dash-dot-dotted), and sum of the kinetic and convective flux $F_C + F_K$ (dashed); (c) source terms due to work done by buoyancy forces P_A, and (d) due to volume changes P_P. The vertical lines enclose the nuclear burning zone (T > 10^8 K).

cally, despite the strong temperature dependence of the energy production rate.

5.1.1. Energy fluxes

Fig. 9 displays the individual contributions of various energy fluxes, time-averaged over many convective turnover times, *i.e.,* only the average effect of convection should be apparent. The derivation of these quantities is explained in Appendix A. All energy fluxes, F, describe the amount of energy which is transported per unit of time across a sphere of given radius.

Most of the nuclear energy production in the convection zone takes place in a relatively narrow shell around the location of the temperature maximum. This energy is transported away by both convection and thermal transport due to heat conduction and radiation. The convective (or enthalpy) flux, F_C, varies from

$-0.2\,10^{42}$ erg s^{-1} up to $1.6\,10^{42}$ erg s^{-1}. The kinetic flux, F_K, reaches a value of at most $1\,10^{42}$ erg s^{-1}, and is mostly positive in the convection zone, *i.e.,* the motion has a predominantly upward direction. This implies that the fast narrow upward directed streams are dominating over the slower and broader downward flows. The ratio of the extreme values of F_C and F_K is nearly 2:1, *i.e.,* nuclear energy is mainly stored in the internal energy of rising hot gas.

Convective and kinetic energy flux together transport more than 90% of the generated nuclear energy upward through the convection zone, the value is dropping to zero towards its border. Part of the heat released in the nuclear processes is in fact transported downwards towards the inner edge of the temperature inversion. Almost none of the nuclear energy reaches the surface of the helium core, neither by convection nor by conduction, *i.e.,* all the energy released is deposited within the core causing
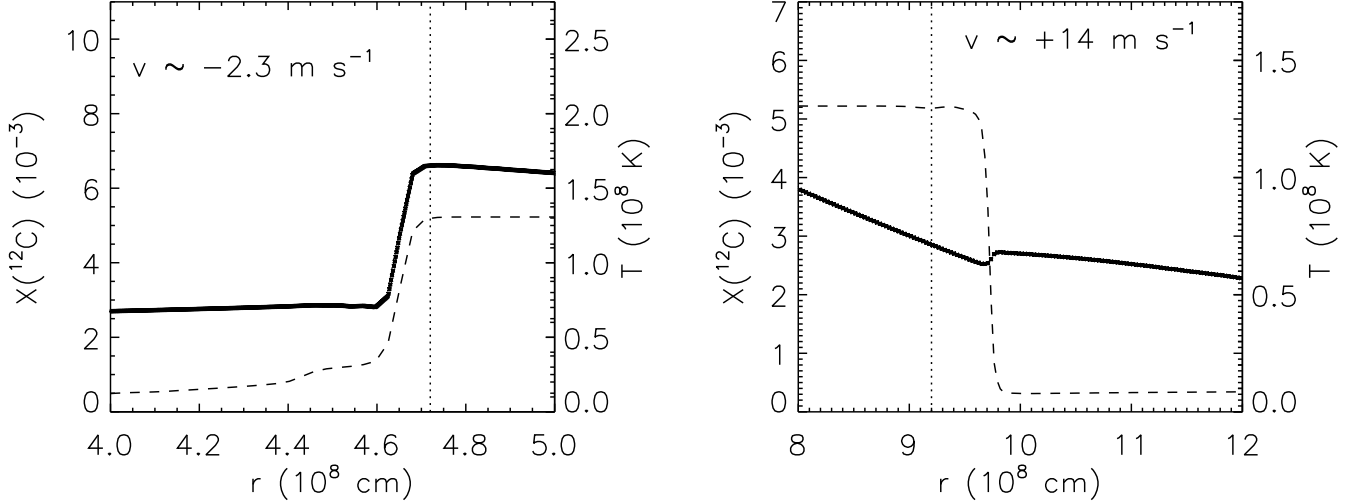
Fig. 10. Angular averaged ^{12}C distribution (dashed) and temperature stratification (thick) at the inner (left panel) and outer edge (right panel) of the convection zone in model DV4 at $t = 30000$ s. The vertical dotted lines mark the initial boundaries of the convection zone at $t = 0$ s.

its expansion. Energy transport due to heat conduction and radiation is everywhere negligible compared to the other contributions. The viscous flux, F_V, is small as well, and losses due to friction, P_V, only influence the dynamics significantly near the borders of the convection zone (Achatz 1995).

For completeness we also consider the flux and source terms of the kinetic energy (see Appendix A), which allow for a further insight into the operation of convection. The radial profile of the source term P_A, corresponding to the work done by buoyancy forces, shows that the vertical convective flows are accelerated due to their density fluctuations in the entire region of dominant nuclear burning (burning zone) above T_{max}. Corresponding pressure fluctuations (causing expansion due to a pressure excess, respectively compression due to a pressure deficit) powered by the volume work P_P show that the gas within the burning region expands, which effectively again implies that an acceleration occurs. Due to the importance of P_P in the convection zone, the acoustic flux F_P, which transports pressure fluctuations, reaches a value comparable to that of the kinetic flux F_K, its value being negligible elsewhere.

5.1.2. Turbulent entrainment, temperature inversion and the growth of the convection zone

Turbulent entrainment (commonly referred to as overshooting) is a hydrodynamic process allowing for mixing and heating in regions which are convectively stable according to the Schwarzschild or Ledoux criterium. Turbulent entrainment, *i.e.*, penetration beyond the formal convective boundaries, takes place at both edges of the convection zone, and is driven by down-flows and up-flows. We study the entrainment by monitoring the temperature changes and the ^{12}C concentration at the (formal) edges of the convection zone. ^{12}C is the most suitable element for investigating the extent of convective mixing, because at the beginning of the simulations, it is mostly absent outside the convection zone, and therefore can be enhanced there only due to overshooting.

At $t = 30000$ s, *i.e.*, near the end of simulation DV4, the temperature inversion is located at $r = 4.65\,10^8$ cm (Fig. 10). Thus, it is about 70 km closer to the center of the star than it was at the beginning of the simulation ($4.72\,10^8$ cm). Its shape remains almost unchanged and discontinuous during the whole evolution, and its propagation speed can be estimated from the heating rate $\delta T/\delta t \sim 2760$ K s^{-1} and the local gradient $\delta T/\delta r \sim 12$ K cm^{-1} at the steepest point of the inversion:

$$\mathrm{v} \simeq -(\delta T/\delta t) / (\delta T/\delta r) \sim -2.3 \text{ m s}^{-1} \qquad (16)$$

This speed is significantly higher than the propagation speed due to the heat conduction alone. Note that the energy flux carried by the heat conduction is seven orders of magnitude smaller than the energy flux carried by the convection. Assuming that the convective energy flux at the position of the temperature inversion ($F_c \sim 0.2\,10^{42}$ erg s^{-1}) is used up completely to heat the layers beneath the temperature inversion, a typical heating rate of $\dot{T} = \dot{E}/C_{inv} \sim 1250$ K s^{-1} can be derived, which is a bit smaller than the value inferred from the simulation, but still in good agreement. C_{inv} is the heat capacity of the layers including the temperature inversion ($C_{inv} \sim 1.6\,10^{38}$ erg K^{-1}). This implies that turbulent entrainment leads to a strong heating of the inner neutrino cooled center of the star that occurs on timescales which are relatively short compared to stellar evolutionary timescales. Such a heating was studied already by Deupree & Cole (1983) and Cole et al. (1985) who obtained qualitatively similar results. Note, that in the one-dimensional stellar evolution calculations the temperature maximum moves outwards with time.

Assuming that the estimated propagation speed of the temperature inversion remains constant, it would reach the center of the helium core and lift the electron degeneracy there in just 24 days. This scenario would rule out the occurrence of mini-flashes subsequent to the main core helium flash, which are observed in stellar evolutionary calculations (Fig. 4). Moreover, as in stars with higher mass and helium abundance the flash occurs closer to the center (Sweigart & Gross 1978), in these stars the center can be reached even faster.

We have also found an influence of the turbulent entrainment on the outer boundary of the convection zone. In the ini-
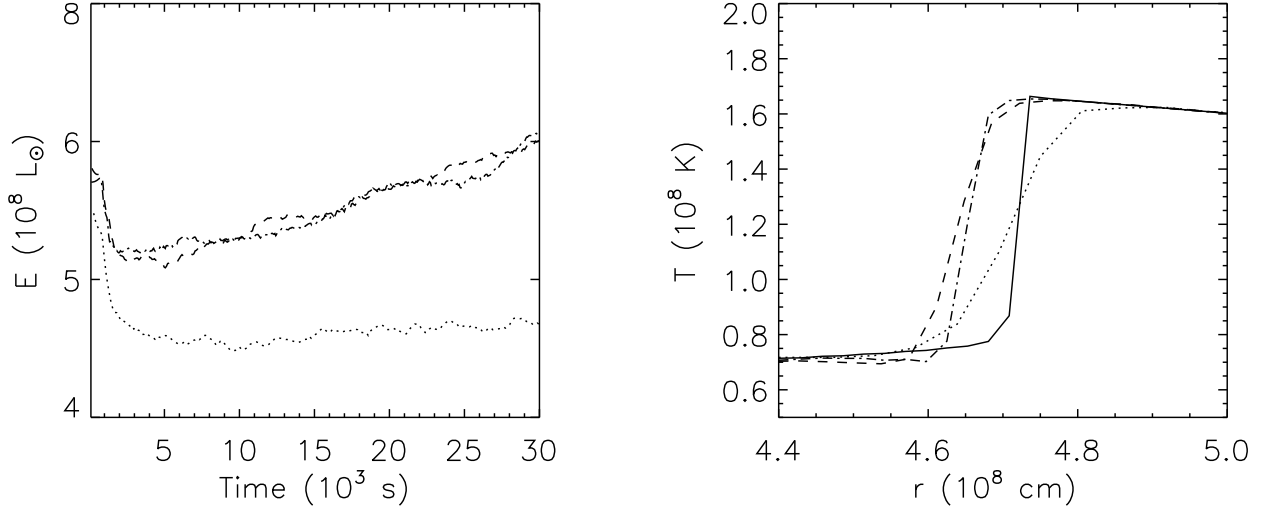
Fig. 11. *Left panel:* Evolution of the total energy production rate in solar luminosity $L_\odot$ for models DV2 (dotted), DV3 (dashed), and DV4 (dash-dotted), respectively. *Right panel:* Mean temperature distribution near the temperature inversion for models DV2 (dotted), DV3 (dashed), and DV4 (dash-dotted) at a $t = 30000$ s, respectively. The initial distribution is shown by the solid line.

tial model this boundary is located at $r = 9.2\,10^8$ cm and corresponds to a discontinuous change in the distribution of elements (Fig. 3), which in stellar evolution models results from the assumed instantaneous mixing. In such models all species in the convectively unstable region are mixed instantaneously across the whole convection zone, while the regions which are assumed to be convectively stable do not experience any mixing at all.

The distribution of ^{12}C at the end of our simulation DV4 is depicted in Fig. 10. Compared to the initial model there is a clear shift of the carbon discontinuity at the outer edge of the convection zone to a larger radius ($r = 9.7\,10^8$ cm). In hydrodynamic simulations the gas overshoots naturally from the convectively unstable to the formally convectively stable region because of its inertia. At the boundaries of the convection zone the overshooting seems always to destroy the stability according to the Schwarzschild criterium transforming the originally convectively stable region into a convectively unstable one. This allows the boundary to propagate further when a subsequent load of gas will try to overshoot at a later time. We have estimated the propagation speed of the outer boundary of the convection zone to be about ~ 14 m s^{-1}. With a propagation speed of this order the convection zone would reach the hydrogen rich layers surrounding the helium core at a radius $r = 1.9\,10^9$ cm and trigger a hydrogen injection flash (Schlattl et al. 2001) within just 10 days. Expected hydrodynamic phenomena due to the extra hydrogen mixing into the helium burning shell via such an extended convection zone could alter the structure of the star significantly. Moreover, additional nucleosynthesis could be triggered, since the hydrogen entrainment will result in the production of neutrons and possibly also of some s-process elements. The hydrogen injection flash in Pop I stars is in contradiction to the canonical scenario since stellar evolutionary models fail to inject hydrogen to the helium core during the core helium flash, unless their metallicity is close to zero (Fujimoto et al. 1990).

Since the turbulent entrainment at the inner convective boundary involved just three radial grid zones over the longest simulations we performed, the estimated propagation velocity must be taken with care and be considered as an order of magnitude estimate. The turbulent entrainment at the outer convective boundary involved eighteen numerical zones in radial dimension, therefore the estimated propagation velocity has higher confidence level, but still it should be taken as a rough number.

5.1.3. Two-dimensional models with different resolution

We find only minor differences between the properties of model DV4 and those of the corresponding models computed with a different grid resolution.

First, the initial mapping process leads to different interpolation errors for different grid resolutions. However, the major source of discrepancy in this phase of the calculation is the stabilization itself. The iterative procedure which minimizes the numerical fluxes across zone boundaries (in order to keep the model in hydrostatic equilibrium) tends to decrease the temperature stronger in models with lower resolution.

Another source of discrepancy is caused by the numerical diffusion which is obviously larger in models with lower resolution. Therefore, model DV2 suffers more from numerical diffusion than model DV3 or DV4, which is evident from Figure 11. The temperature inversion, which is almost discontinuous at the beginning, gets smoothed out faster in model DV2. Note, that the temperature inversion is situated at smaller radii for models with higher resolution, since the typical flow velocities are higher in better resolved models (Tab. 3), *i.e.*, the turbulent entrainment is more effective, and the temperature inversion propagates with higher speed.

Nevertheless, models DV3 and DV4 seem to be well resolved since their mutual differences are minor. The temporal evolution of their total nuclear energy production rate, for instance, overlaps almost perfectly (Fig. 11). The temperature fluctuations in the two-dimensional models are suppressed stronger in the better resolved models. Contrary to Dearborn et al. (2006), the more intense temperature fluctuations occurring in models that we have calculated with grid resolutions even lower than that of model DV2, did not lead to an explosion.

6. Summary

We have presented one and two-dimensional (*i.e.,* axisymmetric) hydrodynamic simulations of the core helium flash near its peak covering about eight hours of evolution time. We find no hydrodynamic events which deviate significantly from the prediction of stellar evolutionary calculations. After an initial adjustment phase the 2D models reach a quasi-steady state where the temperature and nuclear energy production rate are only slowly increasing.

Convection plays a crucial role in keeping the star in hydrostatic equilibrium. Based on our two-dimensional simulation with the highest grid resolution (model DV4), convection follows approximately the predictions of mixing length theory, although the temperature gradient of our dynamically evolved 2D models deviates by about 1% from that of the initial model which is obtained from (1D) stellar evolutionary calculations. The maximum temperature $\langle T \rangle_{max}$ in out best resolved model DV4 rises with a rate of about 40 K s^{-1}, which is about 60% smaller than the rate predicted by stellar evolutionary calculations. The mean convective velocity exceeds the velocities predicted by mixing length theory by up to factor of four.

During the early 2D dynamic evolution the size of the convective region does not deviate from that of the initial (hydrostatic) model. However, after a stable convective pattern is established, our 2D simulations show that the convective flow, consisting of four quasi-stationary large scale ($\sim$ 40 degrees angular width) vortices, starts to push the inner and the outer boundary of the convection zone as determined by the Schwarzschild stability criterium towards the center of the star, and towards the stellar surface, respectively. This results in a rapid growth of the radial extent of the convection zone on dynamic timescales.

Our 2D simulations further suggest that it is unlikely that the core helium flash is followed by subsequent core helium miniflashes, which are observed in (1D) stellar evolutionary calculations, since the inner convective boundary could reach the center of the core in less than one month. On the other hand, the injection of hydrogen from the stellar envelope into the helium core is likely to happen within just 10 days, which is in contradiction to the predictions of the canonical evolution of low-mass Pop I stars.

As our 2D axisymmetric simulations probably cannot properly capture the intrinsically three-dimensional character of the convective flow, we have started to perform also 3D simulations of the core helium flash. In addition, we plan to extend our 2D simulations to time intervals of several days instead of hours. The results of these long-term 2D simulations and of the first well resolved 3D simulations of the core helium flash will be presented in due time elsewhere.

Appendix A: Energy fluxes

An analysis of the vertical energy transport allows for conclusions about the importance of the different physical processes occurring in the convection zone. To separate the various contributions to the total energy flux (Hurlburt et al. 1986; Achatz

1995), one integrates the hydrodynamic equation of energy conservation

$$\partial_t(\rho e) + \partial_i(v_i(\rho e + p) - v_j\Sigma_{ij} - K\partial_i T) = -\rho v_i \partial_i \Phi \quad,$$
$$i, j = 1, 2, 3$$
(A.1)

(with $e = \varepsilon + v_i v_i/2$ being the specific total energy density) over angular coordinates (θ, ϕ), and separates both the specific enthalpy $(\varepsilon + p/\rho)$ and the kinetic energy $(v_i v_i/2)$ into a horizontal mean and a perturbation $(f \equiv \bar{f} + f')$. This results in

$$\partial_t E + \partial_r(F_C + F_K + F_R + F_V + F_E) = 0 \qquad (\text{A.2})$$

with [1]

$$E = \oint \rho e \, r^2 \mathrm{d}\Omega \qquad (\text{A.3})$$

$$F_C = \oint v_r \rho \cdot \left(\varepsilon + \frac{p}{\rho}\right)' r^2 \mathrm{d}\Omega \qquad (\text{A.4})$$

$$F_K = \oint v_r \rho \cdot \left(\frac{1}{2}v_i v_i\right)' r^2 \mathrm{d}\Omega \quad , \quad i = 1, 2, 3 \qquad (\text{A.5})$$

$$F_R = -\oint K\partial_r T \, r^2 \mathrm{d}\Omega \qquad (\text{A.6})$$

$$F_V = -\oint v_i \Sigma_{ri} \, r^2 \mathrm{d}\Omega \quad , \quad i = 1, 2, 3 \qquad (\text{A.7})$$

$$F_E = 4\pi r^2 \overline{v_r \rho} \cdot \left(\overline{\varepsilon + \frac{p}{\rho}} + \overline{\frac{1}{2}v_i v_i} + \partial_r \Phi\right) . \qquad (\text{A.8})$$

Here, the various terms F_i give the total energy transported per unit time across a sphere by different physical processes. They are the convective (or enthalpy) flux, F_C, the flux of kinetic energy, F_K, the flux by heat conduction and radiation, F_R, and the viscous flux, F_V. Finally, F_E, collects all terms causing a spherical mass flow, *i.e.,* the model's expansion or contraction, while F_C and F_K rest on deviations from this mean energy flow (vortices). The latter are the major contributors to the heat transport by convection, while F_V is usually negligibly small.

In a similar way one can also formulate a conservation equation for the mean horizontal kinetic energy, which provides further insight into the effects of convective motions. Using the other hydrodynamic equations

$$\partial_t(\rho) + \partial_i(\rho v_i) = 0 \qquad (\text{A.9})$$
$$\partial_t(\rho v_i) + \partial_j(\delta_{ij}p + \rho v_i v_j - \Sigma_{ji}) = -\rho \partial_i \Phi \quad , \qquad (\text{A.10})$$
$$i, j = 1, 2, 3 \qquad (\text{A.11})$$

and $\partial_t(\rho v_i v_i/2) = v_i \partial_t(\rho v_i) - v_i v_i \partial_t \rho/2$, one finds

$$\partial_t E_K + \partial_r(F_K + F_P + F_V + F_{E,K}) = P_A + P_P + P_V + P_{E,K} \quad (\text{A.12})$$

---

[1] The gravitational potential Φ was assumed to be constant for simplicity.

With F_K and F_V as introduced above, one obtains

$$E_K = \oint \frac{\rho}{2} v_i v_i \, r^2 \mathrm{d}\Omega \tag{A.13}$$

$$F_P = -\oint v_r p' \, r^2 \mathrm{d}\Omega \tag{A.14}$$

$$F_{E,K} = 4\pi r^2 \overline{v_r \rho} \cdot \left(\frac{\overline{p}}{\rho} + \frac{\overline{v_i v_i}}{2} \right) \tag{A.15}$$

$$P_A = -\oint v_r \rho' \partial_r \Phi \, r^2 \mathrm{d}\Omega \tag{A.16}$$

$$P_P = \oint p' \partial_i v_i \, r^2 \mathrm{d}\Omega \tag{A.17}$$

$$P_V = -\oint \partial_i v_j \cdot \Sigma_{ij} \, r^2 \mathrm{d}\Omega \tag{A.18}$$

$$P_{E,K} = 4\pi r^2 \cdot \left(\overline{p \, \partial_i v_i} - \overline{v_r \rho} \, \partial_r \Phi \right) \quad, \quad i = 1, 2, 3 \tag{A.19}$$

where the P_i are source or sink terms of the kinetic energy. They are separated into the effect of buoyancy forces (P_A), friction forces (P_V), and the work due to density fluctuations (P_P, volume changes). By analyzing the various P_i one can determine what brakes or accelerates convective motions. The acoustic flux, F_P, describes the vertical transport of density fluctuations. $F_{E,K}$ and $P_{E,K}$ describe the effect of expansion (volume work, and work against the gravitational potential), similar to F_E in Eq. (A.8).

References

Achatz, K. 1995, in Master thesis, Technical University München
Bader, G. & Deuflhard, P. 1983, Numer. Math., 41, 373
Cole, P. W., Demarque, P., & Deupree, R. G. 1985, ApJ, 291, 291
Cole, P. W. & Deupree, R. G. 1980, ApJ, 239, 284
Cole, P. W. & Deupree, R. G. 1981, ApJ, 247, 607
Colella, P. & Glaz, H. H. 1984, J.Comput.Phys., 59, 264
Colella, P. & Woodward, P. R. 1984, J.Comput.Phys., 54, 174
Cox, A. N. & Stewart, J. N. 1970a, ApJS, 19, 243
Cox, A. N. & Stewart, J. N. 1970b, ApJS, 19, 261
Dearborn, D. S. P., Lattanzio, J. C., & Eggleton, P. P. 2006, ApJ, 639, 405
Deupree, R. G. 1984a, ApJ, 282, 274
Deupree, R. G. 1984b, ApJ, 287, 268
Deupree, R. G. 1986, ApJ, 303, 649
Deupree, R. G. 1996, ApJ, 471, 377
Deupree, R. G. & Cole, P. W. 1983, ApJ, 269, 676
Deupree, R. G. & Wallace, R. K. 1987, ApJ, 317, 724
Dewitt, H. E., Graboske, H. C., & Cooper, M. S. 1973, ApJ, 181, 439
Edwards, A. C. 1969, MNRAS, 146, 445
Fryxell, B., Arnett, D., & Müller, E. 1991, ApJ, 367, 619
Fujimoto, M. Y., Iben, I. J., & Hollowell, D. 1990, ApJ, 349, 580
Hurlburt, N. E., Toomre, J., & Massaguer, J. M. 1986, ApJ, 311, 563
Iben, I. & Renzini, A. 1984, Phys. Rep., 105, 329
Iben, Jr., I. 1975, ApJ, 196, 525
Itoh, N., Hayashi, H., Nishikawa, A., & Kohyama, Y. 1996, ApJS, 102, 411
Kifonidis, K., Plewa, T., Janka, H.-T., & Müller, E. 2003, A&A, 408, 621
Kifonidis, K., Plewa, T., Scheck, L., Janka, H.-T., & Müller, E. 2006, A&A, 453, 661
Lattanzio, J., Dearborn, D., Eggleton, P., & Dossa, D. 2006, ArXiv: astro-ph/0612147
Meakin, C. A. & Arnett, D. 2007, ApJ, 667, 448
Müller, E. 1998, in Lecture Notes in Physics, Berlin Springer Verlag, Vol. 27, Computational methods for astrophysical fluid flow, ed. O. Steiner & A. Gautschy, 343–480
Müller, E., Fryxell, B., & Arnett, D. 1991, in ESO/EIPC Workshop on Supernova 1987A and other Supernovae, p. 99 - 116, 99–116
Müller, E. & Steimnetz, M. 1995, Comp.Phys.Commun., 89, 45
Plewa, T. & Müller, E. 1999, A&A, 342, 179
Porter, D. H. & Woodward, P. R. 1994, ApJS, 93, 309
Potekhin, A. Y., Chabrier, G., & Yakovlev, D. G. 1997, A&A, 323, 415
Press, W. H., Tukolsky, S. A., Vetterling, W. T., & P., F. B. 1992, in Numerical Recipes in FORTRAN, The Art of Scientific Computing, Second Edition (Cambridge: Cambridge University Press), Vol. 1
Rogers, F. J., Swenson, F. J., & Iglesias, C. A. 1996, ApJ, 456, 902
Schlattl, H., Cassisi, S., Salaris, M., & Weiss, A. 2001, ApJ, 559, 1082
Strang, G. 1968, SIAM J.Numer.Anal., 5, 506
Sweigart, A. V. & Gross, P. G. 1978, ApJS, 36, 405
Thomas, H.-C. 1967, Zeitschrift für Astrophysik, 67, 420
Timmes, F. X. & Swesty, F. D. 2000, ApJS, 126, 501
Turkel, E. 1999, Annu. Rev. Fluid Mech., 31, 385
Villere, K. R. 1976, PhD thesis, AA(California Univ., Santa Cruz.)
Weiss, A. & Schlattl, H. 2000, A&AS, 144, 487
Weiss, A. & Schlattl, H. 2007, Ap&SS, 341
Wickett, A. J. 1977, in Lecture Notes in Physics, Berlin Springer Verlag, Vol. 71, Problems of Stellar Convection, ed. E. A. Spiegel & J.-P. Zahn, 284–289
Yakovlev, D. G. & Urpin, V. A. 1980, Soviet Astronomy, 24, 303
Zimmermann, R. 1970, PhD thesis, University of California at Los Angeles, (1970)